IEEE Open Journal of
Vehicular Technology

Received 26 July 2023; accepted 23 August 2023. Date of publication 28 August 2023;
date of current version 11 September 2023. The review of this article was coordinated by Editor Vuk Marojevic.

Digital Object Identifier 10.1109/OJVT.2023.3309103

Investigating UAV Propellers Performances Near Moving Obstacles: CFD Study, Thrust Control, and Battery Energy Management

CHARBEL HAGE, TONINO SOPHY, AND EL-HASSANE AGLZIM

DRIVE Lab, University of Burgundy, F58000 Nevers, France

CORRESPONDING AUTHOR: Charbel Hage (e-mail: charbel.hage@u-bourgogne.fr).

This work was supported by the Bourgogne Franche-Comte region, France (Région BFC) through Deliv'Air Project.

ABSTRACT Quadcopters are widely used in military and civilian applications, but when flying near moving objects, they may encounter flight instability. This study investigates the flow aerodynamic interference of two drones' propellers when they hover near moving obstacles using CFD simulations. An unstructured mesh is used with frame motion to model the propeller's rotation. Different altitudes, rotational speeds, and obstacle velocities are tested to understand their aerodynamic effects on the propeller's performance. The results indicate that hovering 0.1 m above a fixed obstacle at 9550 rpm increased lift by 9.28%. This decreased by half when propellers were positioned adjacent to each other. Besides, a moving wall below the propellers at various velocities significantly affects the thrust and power variation of the propellers at low hovering speeds. For example, when hovering at 3000 rpm over a moving wall at 10 m/s, the thrust on one side of the UAV decreases by 8.51%, leading to flight instability. Different thrust control strategies and flight scenarios are performed to ensure flight stability and energy management. Finally, thrust control strategies prove crucial in stabilizing thrust and altitude, but power consumption increases by 12.8%, requiring 30% more energy required under specific flight scenarios near moving obstacles.

INDEX TERMS Battery management, Computational Fluid Dynamics (CFD), fixed obstacle effect, mesh motion, moving obstacle effect, Multiple Reference Frame (MRF), Phantom DJI 3, power consumption, propellers spacing effect, stability, thrust control, thrust force variation.

I. INTRODUCTION

With the rapid development of unmanned aerial vehicle (UAV) technology, their application in logistics and transportation such as cargo delivery, surface inspections, and military and civilian operations have significantly increased [1], [2], [3], [4], [5], [6], [7]. However, the small size, low cruising speed, and low endurance of these UAVs make them highly susceptible to bad weather, strong winds, and air turbulence, affecting their stability and performance [8], [9], [10], [11]. In addition, the airflow disturbances created by the interference between the quadcopter propeller's downwash flow and fixed or moving obstacles pose a substantial challenge to their operation in urban areas. It is crucial to analyze the aerodynamic characteristics of the quadcopter propeller when operating in the proximity of fixed and moving obstacles, such as walls, cars, buses, and trams. The presence of such obstacles produces complicated flow fields, which can have a major impact on the reliability and stability of quadcopter UAVs. Recent studies have used Computational Fluid Dynamics (CFD) simulations to better understand the aerodynamic behavior of quadcopter propellers in the presence of fixed obstacles, as well as their impact on the UAV's thrust and power consumption. Furthermore, when the UAV approaches moving walls, the incoming airflow generated by the wall's horizontal movement significantly affects the downwash generated by the quadcopter propeller, further complicating the flow field. This, in turn, can impact the stability of the UAV, requiring appropriate thrust control strategies to maintain flight stability and energy management. Thus, investigating the aerodynamic performance of quadcopter UAVs in the presence of fixed and moving obstacles is essential for improving their flight stability in urban areas.

It also highlights the need for effective energy management strategies to ensure that UAVs can operate in such challenging conditions without depleting their battery power rapidly.

At present, the latest theoretical, numerical, and experimental studies examining the ground effect on the thrust of a single propeller do not specifically address the aerodynamic effects of the propellers' interference in the vicinity of fixed and horizontal moving walls. Previous experimental investigations have focused on the effects of rotor rotation, position, blade geometry, and a fixed ground on thrust [12], [13]. The results obtained from the experimental validation of a single quadcopter propeller demonstrate a high level of agreement with the theoretical models proposed by Cheeseman and Bennett in 1955 [14]. It has been observed that the wall effect becomes noticeable when $H/R < 2$ for a single propeller and $H/R < 4$ for a quadcopter (H is the wall height and R is the propeller's radius) [14]. To gain a better understanding of the ground effect on quadcopter performance, several complex theoretical models have been developed based on the Cheeseman and Bennett model. These models have been compared to experimental results, leading to significant progress in predicting the effects of the ground on quadcopter operations. Notably, several authors have made noteworthy contributions in this regard [15], [16], [17], [18], [19], [20]. Additionally, Yao and Hengda conducted numerous experimental and computational fluid dynamics (CFD) studies aimed at optimizing the aerodynamic performance of quadcopters with varying rotor spacing in hovering positions. The results indicate that the aerodynamic performance, including thrust and power, of quadrotors is affected by changes in rotor spacing. Notably, if the rotor spacing is too small or too large, it can negatively impact the hovering efficiency [21].

Computational Fluid Dynamics (CFD) simulations are commonly used to model and predict the 3D flow generated by a specific blade spinning at a particular angular speed. Three methods are commonly used for this purpose: Multiple Reference Frames (MRF), sliding meshes, and dynamic meshes [22]. Among these, the MRF method is often preferred due to its low computational cost, as steady solutions can be obtained without requiring transient simulations. Numerous numerical simulations using the MRF method have been conducted to replicate the flow generated by spinning propellers [22]. The sliding mesh model, unlike the MRF model, requires transient simulations due to the need to update the mesh at each time step. This leads to a significant increase in computational cost. However, the sliding mesh technique offers the advantage of allowing the mesh region around the blade to rotate, which more accurately simulates the actual flow generated by the spinning blade. The studies conducted by [23], [24] on wind turbines' blade performance utilized sliding mesh models. The model consists of a moving region, an external static region, and a sliding interface between the two regions. Unlike the MRF model, the sliding mesh model realistically reproduces the downwash flow by rotating the mesh region containing the propeller blade at a specific speed, causing the blade wall to rotate at the same speed and modify the velocity vector of the fluid cells.

Close to the ground, the MRF model underestimates the thrust compared to the sliding mesh model and the theoretical models proposed by Cheeseman and Bennett [14]. However, the MRF model follows the curvature of the sliding mesh model. The thrust prediction and the ground effect on a single propeller using both methods were studied in detail by [25], and the results showed that the MRF method can accurately predict the thrust and the ground effect with a remarkable reduction of the temporal computational cost compared to the Sliding mesh model. For instance, when considering a simulation with approximately 26 million elements, the MRF model required only around 1000 hours per processor to reach convergence. In contrast, the Sliding mesh model demanded an extensive computational time of 8000–9000 hours per processor until a periodic transient cycle was clearly identified [25]. In addition, examining the magnitude of the MRF thrust normalized by the thrust obtained using the sliding model without the effect of the ground, the results showed also excellent agreement when compared together [25]. Besides, despite showing good agreement the results of the MRF model differ by 9 to 12% with respect to the sliding model [25]. Assuming this deviation, the significantly lower computational cost of the MRF turns this model into a very interesting option. Moreover, MRF has been used in other studies to simulate the flow of a single rotor, yielding good agreement with experimental results [26], [27]. The MRF model was used to analyze the aerodynamic effects on the stability of the flight of a quadcopter UAV in the proximity of walls and ground by Paz et al. [28]. The study aimed to investigate the aerodynamic effects of an obstacle when a quadcopter flies above it at a high rotational speed of 9550 rpm and a high moving velocity of 10 m/s. To ensure precise and reliable analysis, both steady and transient solvers were employed separately. The MRF model specifically employed for the propellers, was used in both solvers. The transient solver was utilized to simulate the drone's horizontal movement above the obstacle, incorporating a dynamic mesh to account for the changing geometry. The obtained results were carefully validated, affirming their accuracy and reliability.

Evaluating the aerodynamic performance of quadcopter UAVs when flying near obstacles is a challenging task due to the multitude of variables involved, such as the shape and size of the obstacle, the distance between the obstacle and the UAV, the speed and orientation of the quadcopter, and the environmental conditions such as wind speed and direction. In addition, the turbulence created by the obstacle speed can significantly affect the stability and control of the quadcopter, making it difficult to predict its behavior accurately. For example, researchers have employed various methods, including wind tunnel tests, to study the flow generated by quadcopter propellers, the impact of the ground effect on induced velocity, and the thrust of the UAV [29], [30], [31]. Besides, 2D and 3D numerical analyses were performed using CFD computational methods and several approaches have been used

to predict the downwash flow of the quadcopter [32], [33], [34], but none of them reproduces the 3D flow generated by the propellers in the presence of a moving obstacle at several altitudes and velocities from the UAV.

Using the commercially available computational fluid dynamics (CFD) solver, FLUENT, the aim of this article is to replicate and assess the interaction between the propellers (29 cm apart) of the Phantom DJI 3 drone and stationary or moving obstacles during hovering flights. That is, how the presence of moving obstacles (car, bus, tram) in the proximity of the propellers affects the fluid flow around the vehicles and the repercussion on the thrust force and power parameters of the propellers (energy management). This scenario is frequently encountered in the project Deliv'Air, which is funded by the Bourgogne Franche-Comté region (Région BFC) and involves the use of delivery drones that can temporarily utilize public transport infrastructure for rapid and autonomous delivery flights. However, during the approach, landing, and take-off phases, the UAV may encounter regions with severe turbulence and fluid separation zones, potentially leading to control instabilities or requiring changes in rotor settings to manage the energy required. Throughout the analyses, an unstructured tetrahedral meshing is used with a k-ω Shear Stress Transport (SST) turbulence model [35]. To consider the rotation of the propeller at various rotational speeds, the Multiple Reference Frame model is employed, taking into consideration both its effectiveness and computational efficiency [36]. Based on the CFD simulations and the thrust control studies, flight scenarios were performed to analyze the power consumption and thrust variation during the hovering and approach phases of the Phantom DJI 3 drone. These flight scenarios take into account the drone's proximity to moving obstacles and the effect on the battery capacity, providing insight into the power and energy consumption of the drone in such situations.

As a result, this contribution is divided into four sections. Following the introduction in Sections I, II presents and provides a detailed explanation of the Deliv'air project, followed by a specific focus on the part subjected to the CFD study to analyze the impact of moving obstacles on the propellers. The geometrical model of the phantom DJI 3 propeller, battery parameters, fluid field partitioning, computational approaches, boundary conditions of each concluded simulation, and flying scenarios are then described in Section III. Section IV then discusses the mesh validation and rotation methods in relation to experimental data. Then, the main results of the study as velocity and pressure fields, aerodynamic parameters, and battery management results are shown and discussed in Section VI. Finally, in Section VIII, the research findings are summarized.

II. DELIV'AIR: SUSTAINABLE GOODS DELIVERY WITH UAVS AND PUBLIC TRANSPORT

The Deliv'Air project intends to create a multimodal transport system that uses drones and the existing public transport system for goods delivery in urban areas, with the goal of reducing CO_2 emissions and fossil fuel consumption. The project involves several phases which are depicted in a scheme in Fig. 1, beginning with the drone carrying parcels from the depot or company warehouse and taking off (1), then climbing to locate a clear and safe path (2) to fly at cruise speed towards the urban area (3). Once in the city, the drone must avoid flying objects and can link to the transport system, such as a bus or tram, that is heading in the direction of the customer to begin the approach phase (4). During the approach and docking phase (5), the drone reduces its performance and hovers at a low height while waiting for the tram, which it lands on while it is in motion. On the tram, the drone charges its battery and reduces its flight duration toward the client.

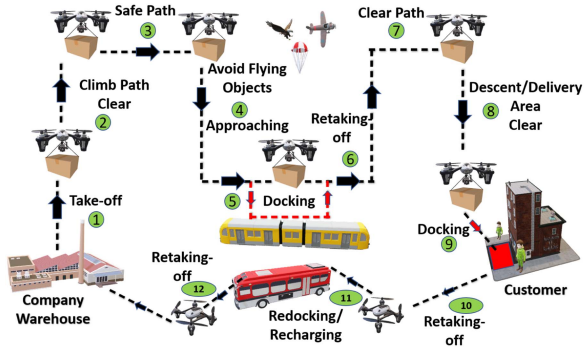

FIGURE 1. Different phases of the Deliv'Air project.

When approaching the client, the drone can take off from the tram to continue its delivery mission (6). The drone flies at a low or high altitude depending on the area (7), and once it arrives at the client's location, it begins its descending phase (8). Finally, as shown in Fig. 1, it hovers in a secure place and docks to deliver the cargo (9).

After finishing the delivery (10), the drone returns to the warehouse for inspection and preparation for another delivery mission. During the return, the drone has the option of docking on a bus or tram going in the direction of the warehouse (11) and then taking off again once approaching or arriving at the desired location (12).

During the different flight phases described above, the drone must be able to adapt to various environmental conditions such as wind, turbulence, and fixed and moving obstacles in the surrounding airspace. For instance, when flying near obstacles like buildings, trees, or vehicles, the performance of the drone's propellers (thrust and power) can be affected by flow disturbances. Therefore, it is crucial to study and optimize the propeller performances in such scenarios to ensure safe and efficient flights.

This study focuses on investigating the impact of moving obstacles on the propellers' performance during the approach and hovering phases (between phases 5 and 6, 11, and 12) of the Deliv'Air project as illustrated in Fig. 2. To achieve this goal, Computational Fluid Dynamics (CFD) simulations are performed to analyze the effect of moving obstacles on the drone's propellers. The results obtained from the CFD

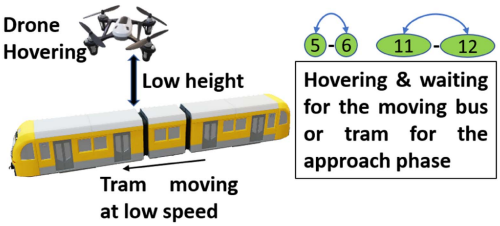

FIGURE 2. Drawing of the specific case investigated in this study.

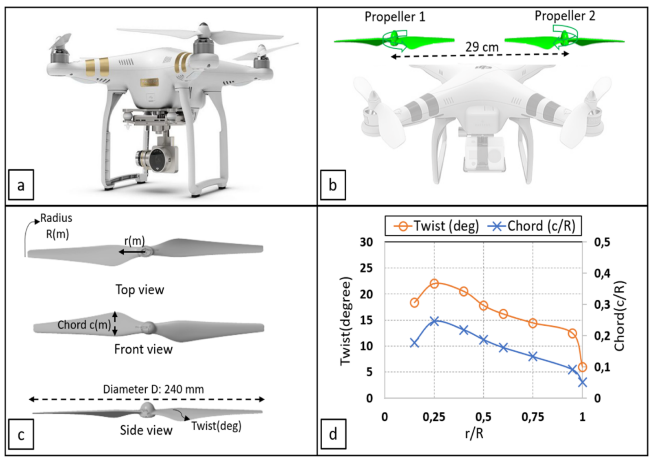

FIGURE 3. Phantom DJI 3 geometry (a) original, (b) CAD model, (c) propeller sketch, (d) propeller dimensions.

simulations are then used to gain insights into the energy management of the drone during different flight scenarios and how to optimize the use of the battery capacity in the presence of obstacles, for ensuring safe and efficient flights.

III. MATERIAL AND METHODS FOR CFD SIMULATIONS

A. PHANTOM DJI 3 DESIGN: 3D GEOMETRICAL MODEL AND DIMENSIONAL SPECIFICATIONS

The Phantom DJI 3 Standard was chosen for this study due to its great popularity and sales in the small quadcopter industry. This UAV has four rotors with diameters of 240 mm each, as well as a camera, mounting assembly, and two support legs, as shown in Fig. 3(a). Besides, the Phantom DJI 3 Standard was chosen for its versatility and endurance in a range of flight scenarios, including urban delivery missions. Because of its small frame and maneuverability, it is a perfect quadcopter for flying in confined locations and near moving vehicles, as in the Deliv'Air project. Its stability and controllability enable accurate navigation and control during the delivery flight.

The CAD model utilized in this CFD study was simplified by reducing the entire geometry to just two drone propellers, positioned 29 cm apart on one side, as shown in Fig. 3(b). This simplification was required to minimize the problem's complexity and make the simulation more viable. The other two propellers' sides were treated as symmetry to the side under consideration, allowing us to minimize the computational cost.

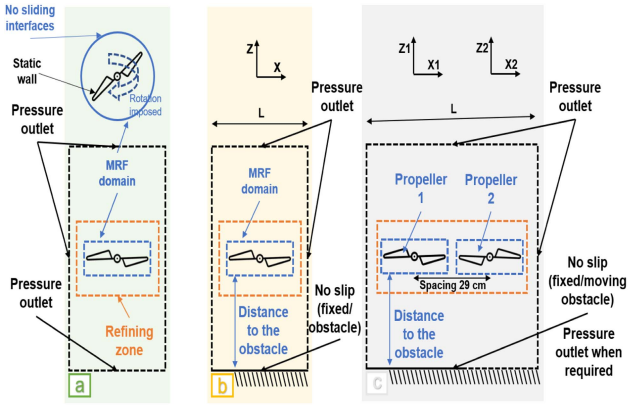

FIGURE 4. Simulation settings used in this study: Schematic representation.

Fig. 3(c) describes the top, front, side view, and shape properties of the propeller 3D model. The graph in Fig. 3(d) shows the chord width and twist angle of the blade along the radius (from the center to the tip), which agrees with the original geometry profile.

It is also important to note that the freight capacity of the Phantom DJI 3 Standard is an essential factor in our study. With the integrated camera and mounting support removed, this UAV can lift an additional 500 g payload (including the battery weight) [37]. Because of its outstanding capacity, it is an ideal choice for a variety of applications, including delivery missions. Finally, the Phantom DJI 3 Standard's flexibility and reliability, combined with its large payload capacity, make it an excellent choice for the Deliv'Air project.

B. NUMERICAL METHODOLOGIES AND BOUNDARY CONDITIONS FOR CFD SIMULATIONS

In this study, three simulation settings were employed to examine each element involved in the interaction between the propellers and a fixed or moving obstacle. These three options (a, b, and c) are presented in Fig. 4 and explained in this section.

The case study shown in Fig. 4 and labeled (a) is used to analyze the flow generated by a rotating propeller, which is an important aspect in simulating a drone's flight. The forces and torques produced are compared to experimental data from reference [38]. Furthermore, mesh convergence is investigated at various rotor speeds in order to identify optimal meshing elements. The Multiple Reference Frame (MRF) rotational approach was used for this investigation and is applied to the fluid environment surrounding the propeller, which is enclosed inside the blue cylindrical domain "MRF domain" [36]. Finally, the trustability and the reliability of the rotational method combined with the meshing quality have been tested against experimental data by estimating the forces exerted by the propeller at different rotational velocities, and the results are shown in Section IV.

The second option, (b), is used to investigate the impact of obstacles on the performance of an isolated propeller. The

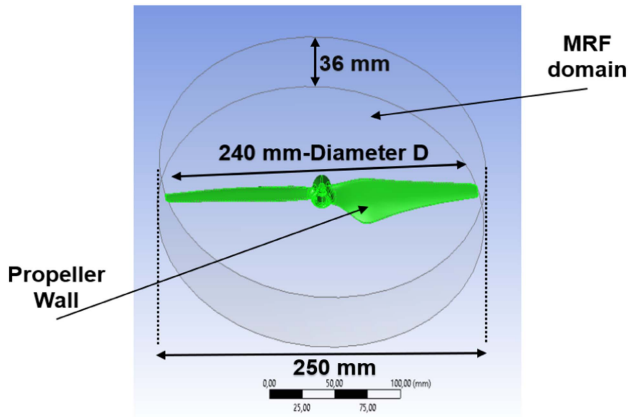

FIGURE 5. Multiple Reference Frame (MRF) fluid domain.

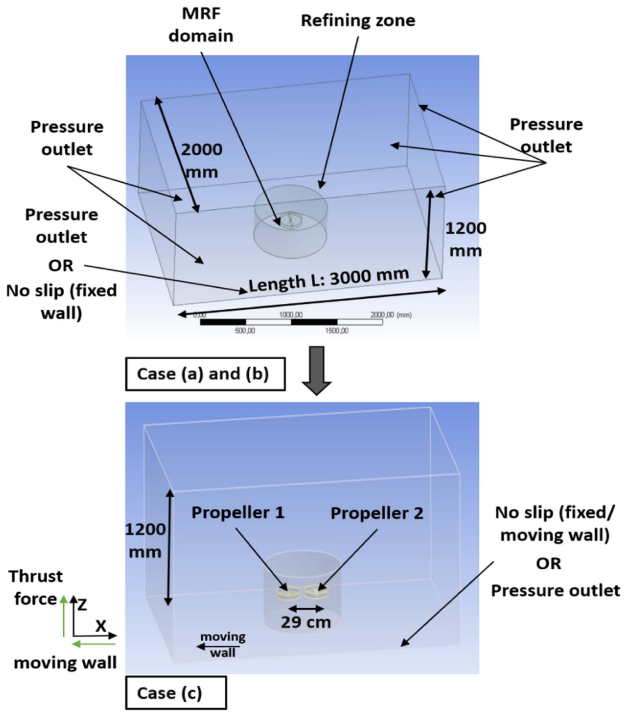

FIGURE 6. Fluid partitioning of domain with propellers: Methodology for isolated propellers (a) and (b) and two propellers (c).

propeller's distance from the wall is gradually reduced (from 1 m to 0.1 m), and the effects of the fixed wall are investigated at various heights and rotating velocities. It is crucial to emphasize that the term "wall" used to describe the boundary condition specifically refers to a smooth surface, such as the roofs of buses and trams in a simplified way (simple wall), as mentioned earlier in the introduction. This simplified planar surface wall approximation is treated in this research and overlooks the actual flow dynamics caused by the tramway roof which is more complex than a planar surface. Furthermore, the wall effect was evaluated at various rotational velocities such as 3000 rpm, 5000 rpm, and 9550 rpm. These rotational values correspond to 25%, 52%, and 80% the maximum rotational speed of the drone motors, respectively. They represent a variety of Phantom DJI 3 standard performance working points, that generate varied thrust forces on the propeller to better investigate the interaction of the downwash with the obstacle at different performance levels.

The third and final case study, labeled (c), investigates the interaction of the propellers with the fixed/moving walls. This CFD simulation analyzes the influence of the propellers' mutual contact as well as the presence of a fixed and moving obstacle. Additionally, the effect of the moving wall on the propellers was studied with different horizontal moving velocities. The obstacle height was constant at 0.2 m, the velocity of the wall was constant at different values (5 m/s, 10 m/s, 15 m/s, and 20 m/s), and the rotational velocity of the propellers was also evaluated at different values (3000 rpm, 5000 rpm, 9550 rpm). It is important to note that the 0.2 m obstacle altitude was chosen as a reference point just before the UAV touches down during the hovering or landing approach.

C. FLUID DOMAIN PARTITIONING AND MESH ELEMENTS

The CAD geometry of the simulation, which includes a phantom DJI 3 propeller with a diameter of 240 mm, is shown in Fig. 5. The overall domain is partitioned into three sections, as illustrated in Fig. 6, the rotational MRF zone, the refining zone around it, and the entire fluid field.

Furthermore, the propeller wall, the rotating MRF domain, and its dimensions are depicted in Fig. 5. The wind field has a total size of a rectangular domain with dimensions of 12.5 × D, 5 × D, and 8.3 × D, where D is the maximum diameter of the propeller. The fluid domain is partitioned in ANSYS software using the Design Modeler, and the meshes are created using ANSYS CFD meshing.

Figs. 5 and 6 show the boundary conditions of the walls surrounding the outer domain, which are set as pressure outlets, no-slip rotating wall, or fixed/moving wall corresponding to the case methodology used (a), (b), or (c), as described previously in Section III-B.

The fluid partitioning of the isolated propeller is illustrated in Fig. 6 cases (a) and (b). Then, the fluid partitioning of the two propellers spaced 29 cm apart is illustrated in Fig. 6 case (c).

Given the efficiency and the tiny relative dimensions of the propeller, an unstructured tetrahedral element was chosen. The inclusion of unstructured tetrahedral elements results in a more precise representation of fluid flow around the propeller and its surroundings. The resulting mesh is shown in Fig. 7, and it contains a total of 922,359 nodes, and 5,222,363 elements for cases (a) and (b) and a total of 1,686,248 nodes and 9,520,895 elements for case (c), where the two propellers are investigated. Besides, a section with a close view of the meshing (c) is also illustrated in Fig. 7.

It is also important to note that before deciding on the mesh quality described previously, mesh independence and convergence investigations were carried out using the methodology

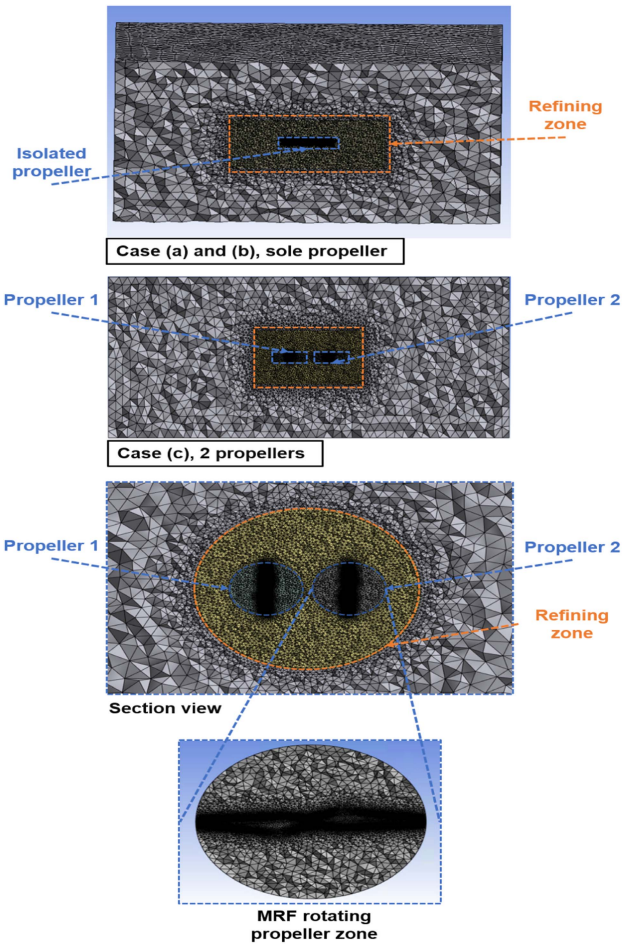

FIGURE 7. Elements of the entire, refining, and propeller fluid domains, (a) and (b) isolated propeller, (c) 2 propellers, section view, MRF domain.

presented in Fig. 4(a). The tests included five variants, as they allowed one to capture the trend and draw conclusions (aspect ratio, orthogonal quality, local minimum size [mm] on the propeller, thrust, and power coefficient). The total number of elements varied from 189,000 to 6 million, as the number of elements along the blade span and blade chord was changed. The sizing of the first layer varied from 3 mm to 10^{-6} mm. Finally, several criteria were also checked to obtain good mesh quality.

D. FLUID DYNAMICS ANALYSIS AND NUMERICAL TURBULENCE MODEL

The fundamental principles of fluid dynamics are the mass and momentum conservation equations, which describe how the parameters of a fluid (density, velocity, and pressure) vary with time. The conservation of mass is described by (1), which states that the rate of change of the fluid's density is equal to the divergence of the density-weighted velocity field [39].

- Mass continuity (Conservation of mass)

$$\frac{\partial \rho}{\partial t} + \left(\rho u_j\right)_{,j} = 0 \tag{1}$$

- Conservation of momentum

$$\frac{\partial \rho u_i}{\partial t} + \left(\rho u_i u_j + p\delta_{ij}\right)_{,j} = \rho f_i + \tau_{ij,j} \tag{2}$$

where ρ, u, and p are the density, the velocity components, and the pressure of the fluid, respectively, τ_{ij} the viscous stress, f_i the external body or volume forces, and t corresponds to time.

The conservation of momentum is described by the (2), which asserts that the rate of change of a fluid's momentum is equal to the sum of external forces acting on the fluid, such as gravitational forces, viscous stresses, and other forces [39]. This equation is used to anticipate the fluid's behavior under various conditions, such as when it is subjected to external forces or encounters obstructions.

The conservation equations in this work are solved using the Reynolds-Averaged Navier-Stokes (RANS), which is a popular method for simulating turbulent flows. For predicting the behavior of turbulence within the flow, the RANS model includes closure equations such as the $k-\varepsilon$ and $k-\omega$ models [40]. The $k-\omega$ SST model, which combines the $k-\varepsilon$ and $k-\omega$ models, is especially successful at forecasting flow separation near the wall and is often used to represent the downwash flow of rotating propellers and machinery, according to [35].

$k-\varepsilon$ model is best suited for flow away from the wall. However, the $k-\omega$ model is best suited for flow near the wall. The SST model is a combination of $k-\omega$ and $k-\varepsilon$. Besides, in the $k-\omega$ model, the wall shear stress is too high and the flow does not separate from the smooth surfaces. Hence, the $k-\omega$ SST model attempts to address and solve these problems and give better separation prediction.

The standard $k-\varepsilon$ model is presented in (3) and (4).

$$\frac{\partial(\rho k)}{\partial t} + \nabla\cdot(\rho \boldsymbol{U} k) = \nabla\cdot\left(\left(\mu + \frac{\mu_t}{\sigma_k}\right)\nabla k\right) + P_k - \rho\epsilon \tag{3}$$

$$\frac{\partial(\rho \epsilon)}{\partial t} + \nabla\cdot(\rho \boldsymbol{U} \epsilon) = \nabla\cdot\left(\left(\mu + \frac{\mu_t}{\sigma_\epsilon}\right)\nabla \epsilon\right) + C_{1\epsilon}P_k\frac{\epsilon}{k} - C_{2\epsilon}\rho\frac{\epsilon^2}{k} \tag{4}$$

with,

$$\epsilon = C_\mu k\omega \tag{5}$$

By substituting in $\epsilon = C_\mu k\omega$ the (3) and (4) we obtain the (6) below.

$$\frac{\partial(\rho\omega)}{\partial t} + \nabla\cdot(\rho \boldsymbol{U}\omega) = \nabla\cdot\left(\left(\mu + \frac{\mu_t}{\sigma_k}\right)\nabla\omega\right) + \frac{\gamma}{\nu_t}P_k - \beta\rho\omega^2 + \underbrace{2\frac{\rho\sigma_{\omega 2}}{\omega}\nabla k : \nabla\omega}_{\text{Additional Term}} \tag{6}$$

where γ and β are constants, σ_{ω^2} is the turbulent Prandtl number for ω, ω is the specific dissipation rate, and Δk and

TABLE 1. Numerical Computational Parameters

Solver type	Pressure-based
Turbulence model	$k-\omega$ SST
Fluid	Air
Blade motion type	Frame motion
Reference frame	Multiple reference frame
Inlet boundary type	Outflow
Outlet boundary type	Outflow
Residual error	$1x10^{-5}$
Pressure-velocity coupling	Simple scheme
Gradient	Least squares cell based
Spatial Discretization (momentum)	Second order upwind
Spatial Discretization (turbulence kinetic energy)	Second order upwind
Spatial Discretization (specific dissipation rate)	Second order upwind

$\Delta\omega$ are the gradients of turbulent kinetic energy and specific dissipation rate, respectively [41].

The $k-\omega$ model equation is presented below in (7).

$$\frac{\partial(\rho\omega)}{\partial t}+\nabla\cdot(\rho\boldsymbol{U}\omega)=\nabla\cdot\left(\left(\mu+\frac{\mu_t}{\sigma_k}\right)\nabla\omega\right)+\frac{\gamma}{\nu_t}P_k-\beta\rho\omega^2 \tag{7}$$

Comparing (6) to (7), all the terms are identical except the additional term.

Moreover, the additional term which exits in the $k-\omega$ model is presented below in (8).

$$2\frac{\rho\sigma_{\omega 2}}{\omega}\nabla k:\nabla\omega \tag{8}$$

This term appears in some turbulence models and represents the effect of the anisotropy of the Reynolds stress on the specific dissipation rate [41]. Multiplying this term by $(1-F_1)$, we obtain the (9) presented below.

$$2(1-F_1)\frac{\rho\sigma_{\omega 2}}{\omega}\nabla k:\nabla\omega \tag{9}$$

where F_1 is a blending function, depends on the local flow conditions, and is typically determined from empirical data depending on the turbulence model used.

Combining the $k-\varepsilon$ and the $k-\omega$ models, the $k-\omega$ shear stress transport (SST) turbulence model has proven its ability to predict flow separation near the wall to reproduce results nearly similar to the experimental ones compared to other turbulence models [35]. Hence, the $k-\omega$ SST model was used in this study to reproduce the downwash flow of the propeller.

Table 1 presents other numerical computational parameters used in the study. The solver type used was pressure-based [42], [43], and Air was the fluid used in the simulations.

As previously mentioned, the blade motion type used for the MRF was the frame motion type to model the rotation of the propeller. Additionally, a simple scheme model was used for the pressure-velocity coupling, and the least squares cell-based method was used for the gradient. Finally, a second-order upwind scheme was used for the spatial discretization of the momentum, the turbulence kinetic energy, and the specific dissipation rate.

Regarding the computational resources, all the simulations were run in parallel on a machine of CPUs with Intel(R) Xeon(R) Silver 4214 processors and 128 gigabytes of RAM. Using the commercial software ANSYS 22.2, all the tests were simulated in a steady state. The average simulation time for each simulation case is 10 hours. Besides, all the results regarding the thrust and power coefficient are averaged around 2 to 3% in case of oscillations and uncertainties during convergence. Averaging the data helps smooth out any fluctuations or uncertainties that may arise during the simulations, enhancing the reliability and accuracy of our findings.

IV. PROPELLER NUMERICAL ROTATIONAL MRF MODEL VALIDATION

To validate the numerical method and the quality of the meshing for reproducing the rotation of the propeller, simulations were run based on experiments published by Deters and Kleinke [38]. In these experiments, a Phantom DJI 3 propeller fixed on a balance that measured thrust and torque was driven by an electric motor. The test findings were provided in terms of the thrust coefficient (C_T) and power coefficient (C_P) for the propeller at various rotational speeds. These coefficients describe the ratio of propeller thrust or power to dynamic pressure or power available in the airflow, respectively. CFD simulations were run to simulate the flow of air around the propeller and determine thrust and power, which were then compared to experimental results using the C_T and C_P equations.

$$C_T=\frac{T}{\rho n^2 D^4} \tag{10}$$

$$C_P=\frac{P}{\rho n^3 D^5} \tag{11}$$

where T is the thrust force, P is the power based on the torque, ρ is the fluid density, n is the rotational velocity, and D is the propeller diameter. Regarding the experimental tests, nD is used as the reference velocity and D^2 as the reference area.

In terms of simulations, the phantom DJI 3 propeller was assessed at five different rotational speeds within the experimental range, as shown in Fig. 8. The C_T, and C_P CFD results of the simulations are dotted in red Diamond and green Plus sign, respectively. The simulations were carried out for the isolated propeller and for the two propellers (spaced 29 cm apart) separately following the methodology cases (a) and (b) presented previously in Section III-B. The results for both cases follow the same behavior and show good agreement with the experiment data by Deters and Kleinke [38] and with the CFD results by Paz et al. [28].

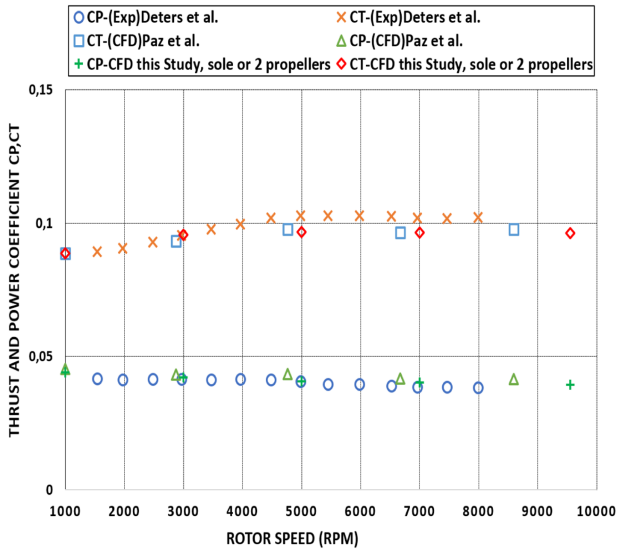

FIGURE 8. Validation of the propeller rotation methodology.

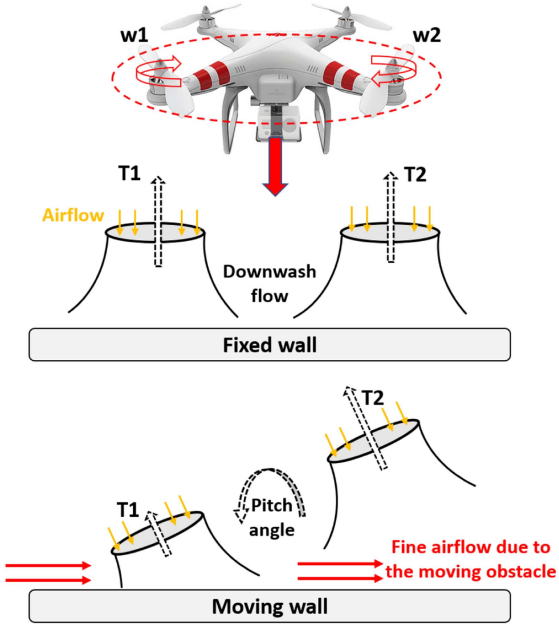

FIGURE 9. Aerodynamic behavior in the presence of moving obstacles.

The CFD results of this study underestimate the thrust coefficient for rotation velocity higher than 4000 rpm. However, this underestimation is inferior to 8% compared to the experiment data [12]. Besides, the CFD results of this article follow the same curve of both the experimental data and the CFD results by Paz et al. [25]. Therefore, the rotation methodology as well as the mesh performance used in this study are considered suitable to reproduce the reaction force tested by the propeller due to the airflow generation.

V. THRUST FORCE CONTROL AND BATTERY ENERGY MANAGEMENT

A. THRUST CONTROL AND PITCH ANGLE CORRECTION

Compared with the fixed obstacle case, the variation in the aerodynamic behavior of the two propellers is determined by the interference of the downwash and the airflow generated by the moving obstacle. Considering that the variation in the UAV's thrust and power is mainly caused by the moving obstacles below the propellers and the interactions between the downwash flows, the stability and flight efficiency of the UAV are challenged in hovering and approaching conditions. Fig. 9 shows the aerodynamic behavior of a UAV in hovering conditions over fixed and moving walls.

When operating in close proximity to moving walls with a specific horizontal velocity, the quadcopter can become severely unstable. The propeller that faces the airflow is typically the one that experiences a decrease in thrust, leading to a change in the quadcopter's pitch angle. This behavior is illustrated in Fig. 9. To compensate for the reduction in thrust on the propeller facing the airflow (propeller one), a backward calculation method is used to compute the new thrust amount (then consumption) required to stabilize the UAV and reduce its pitch angle. For example, if the propeller is rotating at 3000 rpm, the thrust reduction caused by the moving obstacle is taken into account to determine the actual rotational velocity of the propeller. This reduced value is added to the normal rpm to compensate for the decrease in thrust.

Finally, the aerodynamic behavior and thrust control strategies are studied and predicted through the CFD methodologies presented previously. The results will be presented and explained in detail in the results section.

TABLE 2. Phantom DJI 3 Standard Battery Specifications

Battery type	Capacity (mAh)	Voltage (V)	Energy (Wh)
LiPo 4S	4480	15,2	68

B. SPECIFICATIONS OF THE PHANTOM DJI 3 STANDARD BATTERY

As previously stated, we will evaluate the energy consumption of the UAV under various flying circumstances using power and thrust data acquired from computational fluid dynamics models. To accomplish this, we will need information regarding the Phantom DJI 3, which will be included in our research.

The specifications of the phantom DJI 3 battery are presented in Table 2 [37]. It is a 15.2 V 4480 mAh LiPo battery with a charging capability of 68 W. Besides, it is developed exclusively for use with the Phantom 3 Standard drone and offers up to 25 minutes of flight time on a single charge [37].

The battery image is presented in Fig. 10, which is sourced from [44].

These specifications combined with power consumption obtained from the CFD study will be used to calculate the battery energy consumption level of the drone when operating under different flight scenarios.

FIGURE 10. Phantom DJI 3 battery.

C. HOVER AND APPROACH FLIGHT SCENARIOS

Four flight scenarios for flying at cruise speed towards the city, hovering, and approaching the moving vehicle are presented below. Based on these scenarios and the CFD data, the battery energy consumption level can be managed and assessed carefully for a safe delivery flight.

- *Scenario 1:* The phantom DJI 3 is cruising during 10 minutes flight towards the city and has 60% battery performance remaining. Upon reaching the destination (time to dock on a tram), the quadcopter hovers at 5000 rpm for 2 minutes while waiting for a moving tram or bus. Once the tram arrives, the quadcopter approaches it at 3000 rpm (propeller's rotation speed) a total of 4 times, each time for 30 seconds, for a total of 120 seconds. It is expected that the quadcopter approaches 4 trams during its delivery flight. It is vital to note that in this scenario, the thrust control of the propellers to stabilize the UAV is not taken into consideration. The total hovering and approach time for scenario 1 is 4 minutes.
- *Scenario 2:* This scenario is similar to the first one, with the same 10-minute cruising flight towards the city and 60% battery performance remaining. However, an additional 60 seconds are added to the approach phase for control and stability, with 15 seconds added to each approach. This means that each approach now takes 45 seconds instead of 30 seconds. Moreover, in this scenario, the increase in power when the thrust is controlled is taken into consideration during the approach phase to ensure stable flight. The total hovering and approach time for scenario 2 is 5 minutes.
- *Scenario 3:* This scenario is similar to the second one. However, an additional 60 seconds are added to the approach phase for enhancing control and stability, with 15 seconds added to each approach. This means that each approach now takes 60 seconds instead of 45 seconds. The total hovering and approach time for scenario 3 is 6 minutes.
- *Scenario 4:* This scenario is similar to scenario 3. However, during the fourth approach, the quadcopter was unable to complete it and had to hover for an additional 40 seconds before attempting the fourth approach again with 45 seconds (as in scenario 2). The total hovering and approach time for scenario 4 is 7 minutes and 25 seconds.

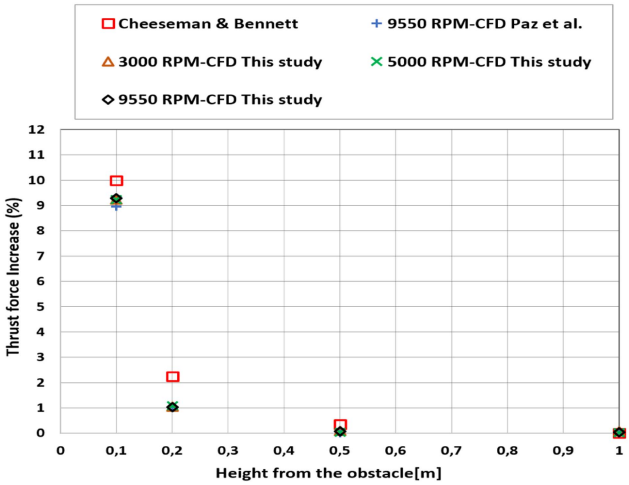

FIGURE 11. Effect of fixed obstacle proximity on an isolated propeller.

As presented in the previous scenarios, each flight phases require additional time for the quadcopter to complete the approach. This can impact the overall delivery time and battery performance and must be taken into consideration for the deliv'Air delivery missions. Finally, the results of the battery consumption level related to each scenario are presented in the results section.

VI. CFD RESULTS AND DISCUSSION

A. EFFECT OF FIXED OBSTACLE ON ISOLATED PROPELLER

Following the validation of the mesh and the numerical approach for recreating the propeller's rotation, the impact of an obstacle's close proximity on the propeller was explored using additional simulations. Thus, a solid wall was placed at various distances below the propeller, and simulations were run at various rotational speeds (3000, 5000, and 9550 rpm) while preserving the same boundary conditions for the outer domain's walls (pressure outlet). Furthermore, the results for the three rotating speeds were compared to a mathematical model based on the image approach, as defined by Cheeseman and Bennett in [14].

$$\frac{T}{T_\infty} = \frac{1}{1 - \left(\frac{R}{4z}\right)^2} \tag{12}$$

where R is the propeller radius, z is the vertical distance measured from the obstacle, T is the thrust generated by the propeller when the obstacle is present, and T_∞ is the thrust generated by the propeller in the absence of the obstacle. The three velocities conditions employed in the simulations allow the CFD methodology and theoretical model to be considered and valid at any rotational speed.

The results are depicted in Fig. 11, where the thrust force increase is graphed at different heights from the obstacle and for different rpm. The thrust force increase percentage is calculated using this formula (T-T_∞)/T_∞.

Cheeseman and Bennett's theoretical model results are dotted in red squares. Furthermore, the CFD simulations of this

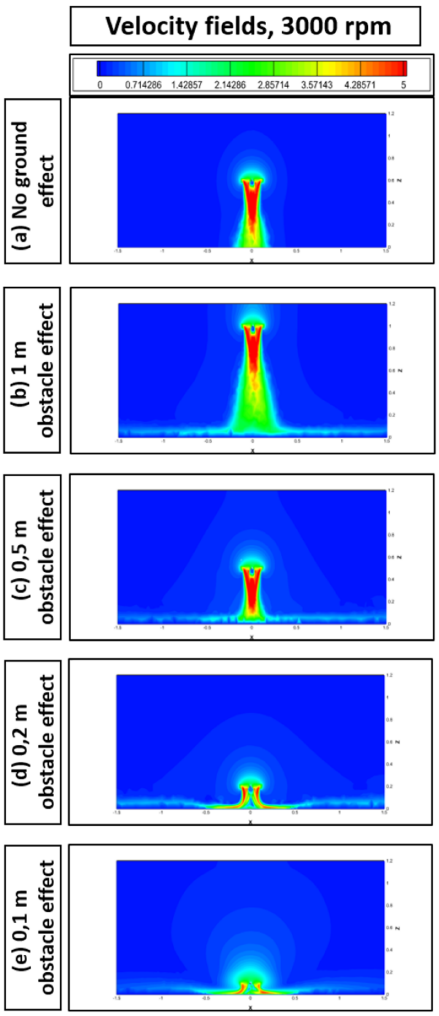

FIGURE 12. Velocity fields of an isolated propeller (3000 rpm), at different obstacle heights (no ground, 1 m, 0.5 m, 0.2 m, 0.1 m).

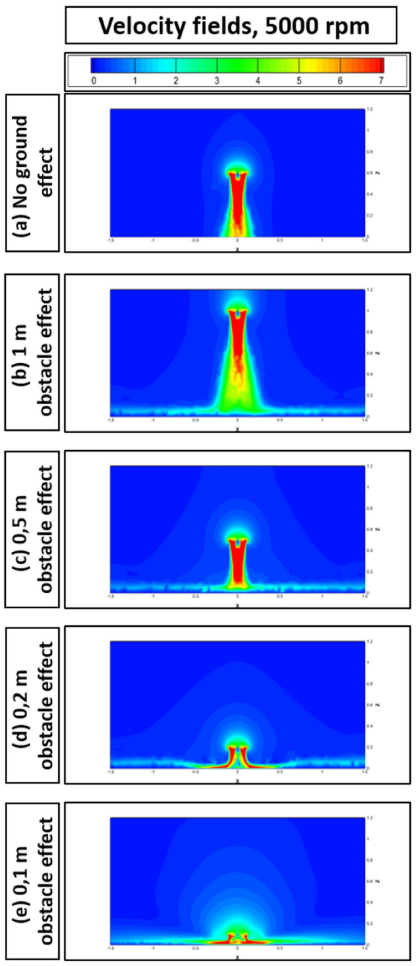

FIGURE 13. Velocity fields of an isolated propeller (5000 rpm), at different obstacle heights (no ground, 1 m, 0.5 m, 0.2 m, 0.1 m).

work, the CFD simulations of Paz et al., and the theoretical data all follow the same curve, however, both CFD findings underestimate the thrust created by the propeller at 0.1 m and 0.2 m from the fixed wall by roughly 1%.

Besides, the velocity fields of the propeller at 3000 rpm, 5000 rpm, and 9550 rpm in the presence of the fixed obstacle are shown in Figs. 12, 13, and 14, respectively. The effect of the wall is compared to the no-ground effect (a) at various height proximities. The fluid tube created by the propeller has no ground contact (a) and flows freely downwards in a symmetrical and rectilinear course.

The reason for the propeller thrust increase at 0.1 m and 0.2 m from the obstacle is illustrated in Figs. 12, 13, and 14(d) and (e) for the three rotational speeds. The obstacle located in close proximity to the propeller causes the flow tube to diverge radially, increasing the thrust. Furthermore, as the wall goes away from the propeller, the tube flow is unaffected and remains steady and symmetrical, as illustrated in the figures for situations (b) and (c).

B. EFFECT OF FIXED OBSTACLE ON TWO PROPELLERS

After studying the effect of a fixed obstacle on an isolated propeller, the effect of two propellers placed close to each other (spacing 29 cm) was studied, and the results were compared to Cheeseman and Bennett's theoretical model and the CFD results of this study corresponding to an isolated propeller.

The simulations were conducted at different wall altitudes, and rotational speeds (3000 rpm, 5000 rpm, and 9550 rpm). The results for two propellers spaced 29 cm apart and rotating at 9550 rpm are shown in Fig. 15.

The results demonstrate that a 29 cm gap impacts the downwash of both propellers 1 and 2, reducing thrust by 4% at 0.1 m and 0.36% at 0.2 m. At a low distance from the wall, the propeller interference prevents the adequate generation of downwash, causing the flow to be partially disturbed. This interruption of the downwash can have a relatively small effect on the flow around the propellers, potentially affecting the quadcopter's stability and performance.

In addition, the velocity fields of the propellers rotating at 3000 rpm, 5000 rpm, and 9550 rpm in the presence of the obstacle are shown in Figs. 16, 17, and 18, respectively.

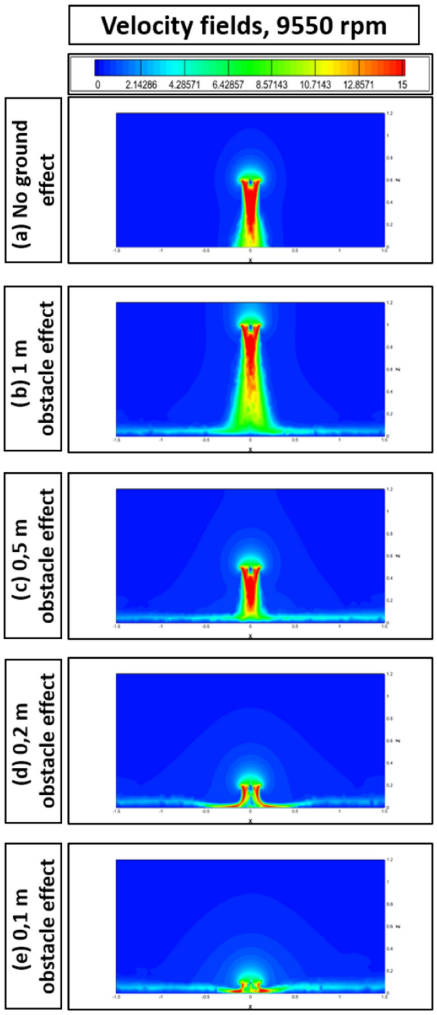

FIGURE 14. Velocity fields of an isolated propeller (9550 rpm), at different obstacle heights (no ground, 1 m, 0.5 m, 0.2 m, 0.1 m).

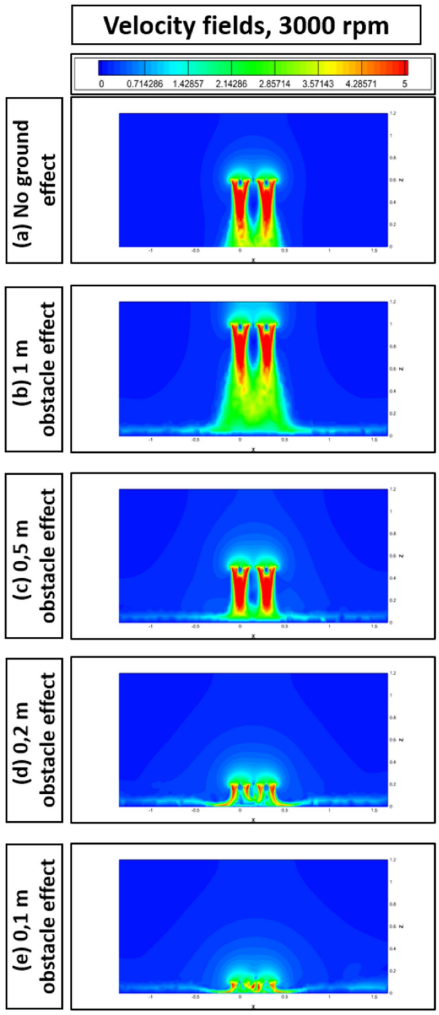

FIGURE 16. Velocity fields of the two propellers (3000 rpm), at different obstacle heights (no ground, 1 m, 0.5 m, 0.2 m, 0.1 m).

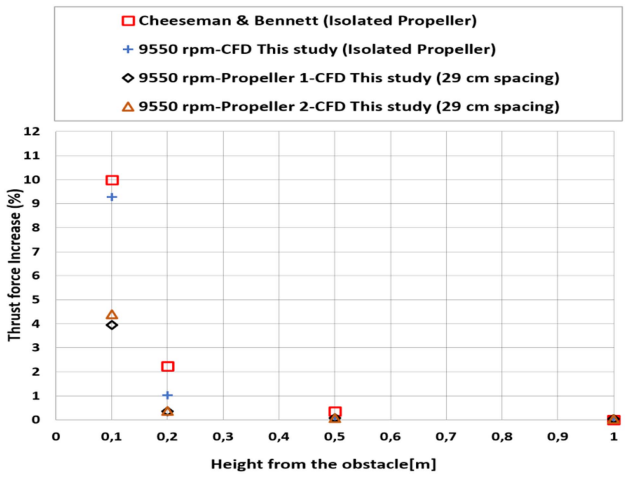

FIGURE 15. Effect of fixed obstacle proximity on two propellers.

The impact of the wall is compared to the case when there is no ground effect (a). The flow of fluid produced by the propellers is not blocked by the ground in this situation, and it follows a symmetrical and straight downward way. The increase in propeller thrust at 0.1 m and 0.2 m from the obstacle is shown in Figs. 16, 17, and 18(d) and (e).

As a wall is positioned near the propellers, the flow diverges radially, changing the direction of the downwash in between the propellers, causing the flow to separate and resulting in a drop in thrust as compared to an isolated propeller scenario.

As the propellers move away from the wall (cases (b) and (c)), the tube flow is unaffected, and the interference is weaker than in cases (d) and (e).

C. MOVING OBSTACLE EFFECT ON TWO PROPELLERS (3000 RPM) AND THRUST CONTROL

The last three steps of this study were the evaluation of the moving obstacle effect on the propeller hovering at 3000 rpm,

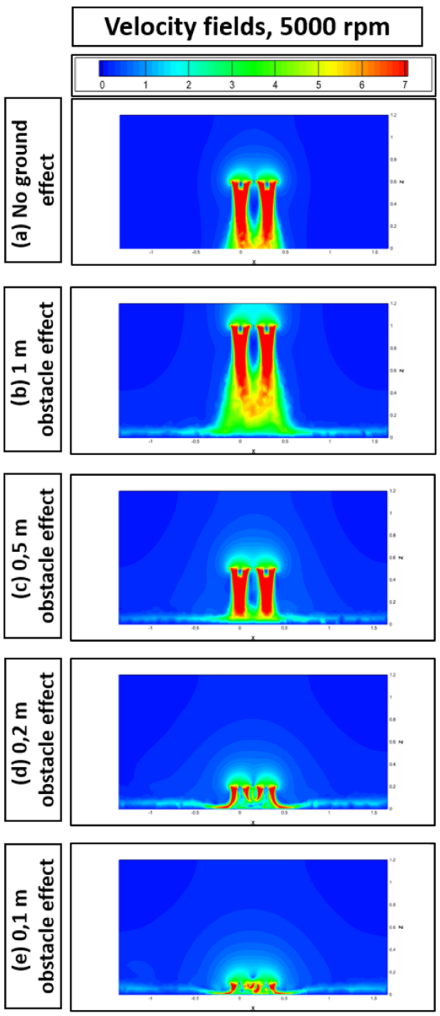

FIGURE 17. Velocity fields of the two propellers (5000 rpm), at different obstacle heights (no ground, 1 m, 0.5 m, 0.2 m, 0.1 m).

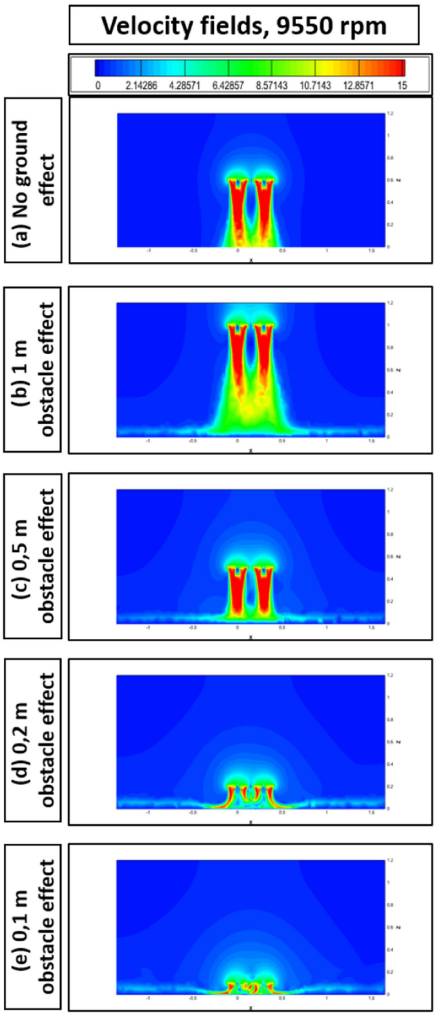

FIGURE 18. Velocity fields of the two propellers (9550 rpm), at different obstacle heights (no ground, 1 m, 0.5 m, 0.2 m, 0.1 m).

5000 rpm, and 5990 rpm at 0.2 m from the obstacle, as it happens when the drone is hovering at a specific altitude waiting for a moving vehicle to approach (train, bus, or car). This study solely focuses on the hovering phase above the moving object. The CFD calculations were carried out with four horizontal velocities of the obstacle in consideration and the fixed obstacle case was used as a comparison reference (0.36% thrust effect on the propellers). The thrust force variation on the propellers hovering at 3000 rpm is shown in Fig. 19. The results have shown an increase in the lift for propeller 1 by 0.4%, and for propeller 2 by 0.07% at 5 m/s moving obstacle and then a decrease for propeller 1 by 8.5% and 10.7% at 10 m/s, and 15 m/s, respectively, compared to fixed obstacle thrust (0 m/s). However, propeller 2 maintained its thrust when the obstacle is moving at 5 m/s and 10 m/s, and then starts decreasing by 4.7% and 7% at 15 m/s, and 20 m/s, respectively. It is also evident that propeller 1 experiences a significant increase in thrust when the wall moves at 20 m/s,

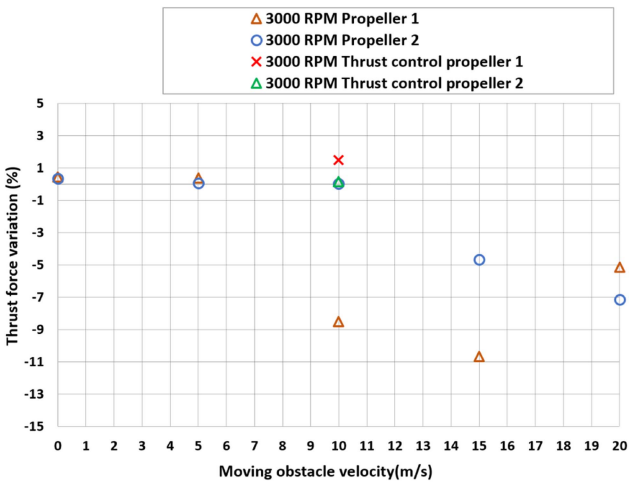

FIGURE 19. Effect of moving obstacle proximity (0.2 m) on the thrust of propeller 1 and 2 (3000 rpm).

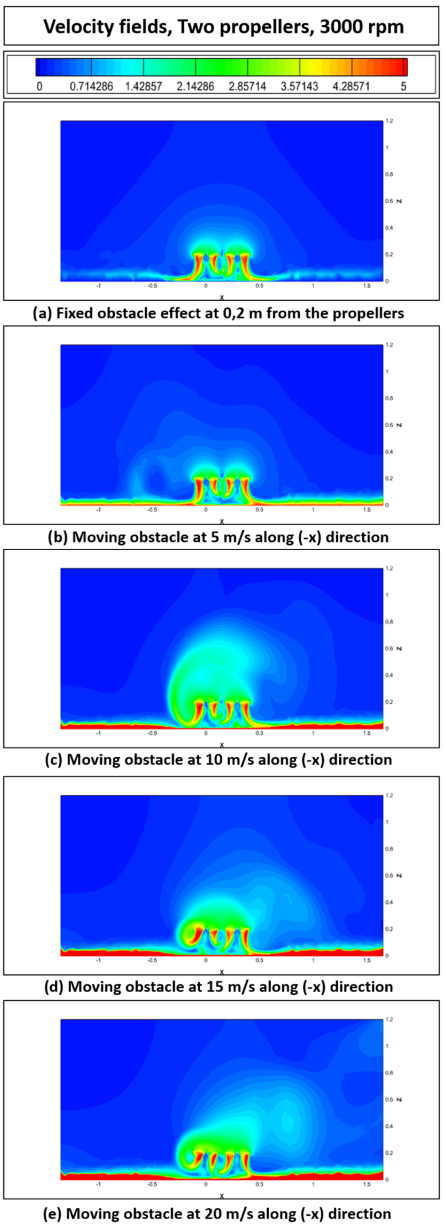

FIGURE 20. **Velocity fields, 2 propellers 3000 rpm, effect of moving obstacle 5 m/s, 10 m/s, 15 m/s, and 20 m/s.**

surpassing the thrust generated by propeller 2. This aerodynamic phenomenon and sudden increase in thrust, following a 10.7% decrease at 10 m/s, can be explained by analyzing the velocity and pressure contour presented below.

The cause of the difference in thrust for both propellers near a moving wall is presented in Fig. 20(a)–(d), where the velocity fields of the propellers rotating at 3000 rpm are presented in detail. Fig. 20(b) depicts the flow over the obstacle moving at 5 m/s in the (x) direction, as well as the downwash generated by the propellers in both directions (x) and (−x). On the left side of the downwash (propeller 1), the flows conflict with each other, and a small separation zone appears far from the propeller ($x = -0.5$ m), causing the thrust to slightly rise on both sides. Besides, the strong interference between the downwash and the flow generated by the moving obstacle begins to intensify at 10 m/s.

Fig. 20(c) depicts the flow over the wall traveling at 10 m/s in the (x) direction, as well as the downwash generated by the propeller in both directions (x) and (−x). On the left side of the propeller, the flows aggressively interact with one another and on the left side of the propeller 1 and a massive separation zone forms, causing the thrust to drop by 8.5%. It is critical to note that propeller 2 is shielded from thrust fluctuation by propeller 1, and the downwash is not adversely influenced by the moving wall. This unbalanced aerodynamics on one side of a UAV can cause a massive pitch angle, leading to instability and a possible crash unless swift thrust control is applied to stabilize the quadcopter's trajectory. Therefore, a thrust control was applied during this stage of the CFD study to investigate the effect of increasing the rpm on propeller 1 to compensate for the decrease in thrust. This approach aligns with the thrust control strategy discussed in Section V-A. The reduction in the rotational speed of propeller one is calculated based on the new thrust value (which decreased by 8.5%), using the thrust coefficient equation presented earlier. To counterbalance the decrease in thrust, the reduced rotational speed is added to 3000 rpm, compensating for the drop caused by the moving obstacle. The outcome of the thrust control strategy is presented in Fig. 19, where the red cross marker represents the newly estimated thrust value for propeller 1. Following the thrust control, the balance on both sides of the quadcopter is corrected and stabilized, resulting in an approximate 9% increase in the propeller one thrust.

Fig. 20(d) depicts the flow over the obstacle traveling at 15 m/s in the (x) direction, as well as the propeller downwash generated in both the positive and negative x-directions. On the left side of the downwash and between the propellers, the flows marginally interact with each other, resulting in a significant separation zone adjacent to propeller 1. This causes a significant decrease in thrust by 4.7% and 10.7% on propeller 1 and propeller 2, respectively.

Fig. 20(e) illustrates the effect of an obstacle moving at a velocity of 20 m/s in the x-direction on the flow of a propeller rotating at 3000 rpm. The downwash generated by the propeller creates a zone of interference on the left side (propeller 2), leading to a severe separation zone that causes a decrease of 7% in the thrust of propeller 2. However, the thrust on propeller 1 increases by 6% compared to the previous case (decrease by 10.7% over 15 m/s moving wall). This increase in the thrust is explained using the pressure contours illustrated in Fig. 21.

The pressure contours in Fig. 21 reveal that the pressure beneath propeller 1 is lower when a moving obstacle travels at 15 m/s compared to when it moves at 20 m/s. Specifically, the pressure contour beneath propeller 1 indicates a value of 3.4 Pa for the 15 m/s moving obstacle and 15.8 Pa for the 20 m/s moving obstacle. This difference in pressure beneath the propeller results in an increase in thrust, as shown in the graph presented in Fig. 19.

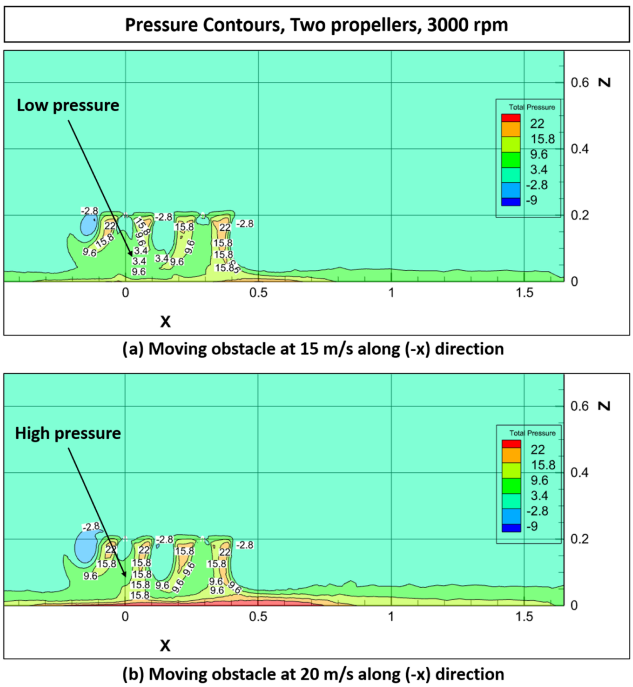

FIGURE 21. Pressure contours, 2 propellers 3000 rpm, effect of moving obstacle 15 m/s and 20 m/s.

D. MOVING OBSTACLE EFFECT ON TWO PROPELLERS (5000 RPM) AND THRUST CONTROL

A parametric investigation was conducted to study the aerodynamic performance of propellers in the presence of a moving wall when hovering at 5000 rpm. This study aimed to improve understanding of the UAV's aerodynamic behavior when operating at different power loadings. When the quadcopter carries a heavier payload, it must hover at a higher rotational speed to ensure a safe delivery flight. The CFD simulations have been performed considering four horizontal velocities of the wall and the fixed obstacle case was taken as a comparison reference (0.36% thrust effect on the propellers). The thrust force variation on the propellers hovering at 5000 rpm is shown in Fig. 22. The results have shown an increase in the lift for propeller 1 and propeller 2 by 0.4% at 5 m/s moving obstacle and then a decrease for propeller 1 by 2% and 5% at 10 m/s, and 15 m/s, respectively, compared to fixed obstacle thrust (0 m/s). However, propeller 2 also maintained its thrust when the obstacle is moving at 5 m/s and 10 m/s with a slight decrease, and then starts slightly decreasing by approximately 0.8% at 15 m/s, and 20 m/s. Similar to when it is hovering at 3000 rpm, propeller 1 experiences also a slight increase in thrust when the wall moves at 20 m/s. This aerodynamic phenomenon and sudden increase in thrust, following a 5% decrease at 10 m/s, can be explained by analyzing the velocity and pressure contour presented below. Besides, it is noticeable that the effect of moving walls at low velocities on the thrust is almost negligible when the propeller is hovering at 5000 rpm. However, the thrust is still affected when the wall is moving at high speed.

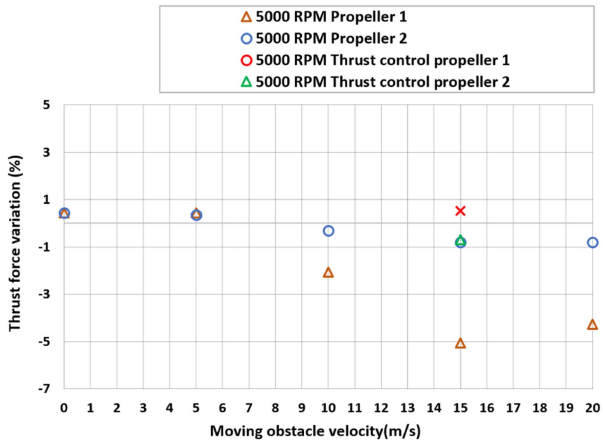

FIGURE 22. Effect of moving obstacle proximity (0.2 m) on the thrust of propeller 1 and 2 (5000 rpm).

The cause of the difference in thrust for both propellers near a moving wall is presented in Fig. 23(a), (b), (c), (d), and (e) where the velocity fields of the propellers rotating at 5000 rpm in the proximity of moving walls are presented in detail. Fig. 23(b) depicts the flow over the obstacle moving at 5 m/s in the (x) direction, as well as the downwash generated by the propellers in both directions (x) and (−x). The flows interfere with each other slightly on the left side of propeller 1 and between the propellers, resulting in a minor fluctuation in thrust. It is also visible that the downwash separation is moving further from the propeller compared to the hovering speed of 3000 rpm.

Fig. 23(c) depicts the flow over the wall moving at 10 m/s in the (x) direction, as well as the downwash generated by the propellers in both directions (x) and (−x). On the left side of the downwash, the flows somewhat interact with each other, and a small separation zone appears close to the propeller, causing the thrust of propeller 1 to fall by 2% while propeller 2 is protected.

Fig. 23(d) shows the flow over the obstacle moving along (x) direction at 15 m/s, and the downwash of the propeller generated in both the positive and negative x-directions. The flows strongly interfere with each other on the left side of the downwash, resulting in a large separation zone next to propeller 1, and causing a significant decrease in thrust by 5%. Besides, propeller 2 is slightly affected at this stage and experiences a decrease in thrust of 0.7%. It is noticed at 5000 rpm that the effect of the moving wall is pushed further to higher velocities (15 m/s and 20 m/s) compared to when the propellers are hovering at 3000 rpm. At 15 m/s, the same aerodynamic behavior occurs on one side of a UAV causing a pitch angle, leading to instability and a possible crash. Therefore, a thrust control was also applied during this stage of the CFD study to investigate the effect of increasing the rpm on propeller 1 to compensate for the decrease in thrust. To counterbalance the decrease in thrust, the reduced rotational speed is added to 5000 rpm, compensating for the drop caused by the

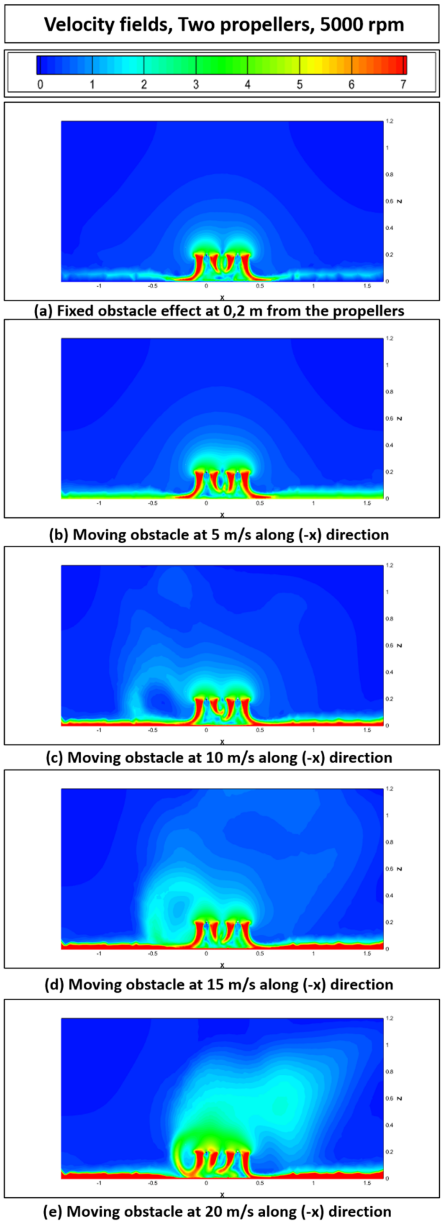

FIGURE 23. Velocity fields, 2 propellers 5000 rpm, effect of moving obstacle 5 m/s, 10 m/s, 15 m/s, and 20 m/s.

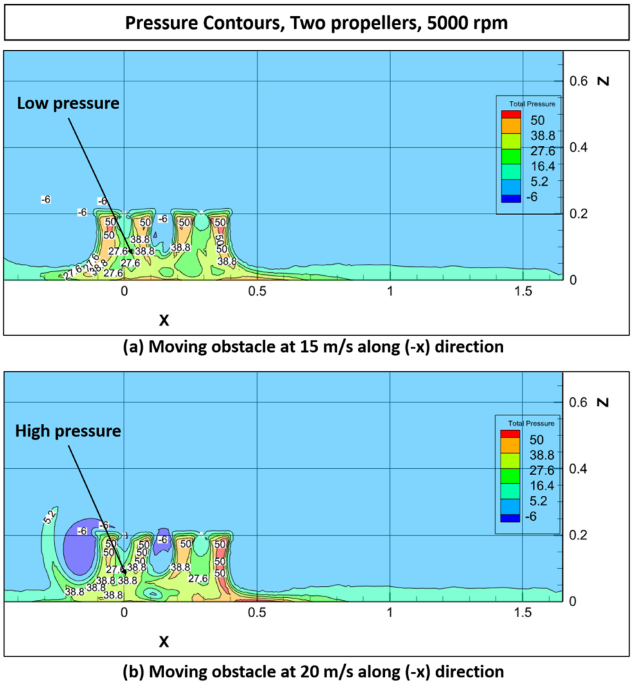

FIGURE 24. Pressure contours, 2 propellers 5000 rpm, effect of moving obstacle 15 m/s and 20 m/s.

moving obstacle. The outcome of the thrust control strategy is presented in Fig. 22, where the red cross marker represents the newly estimated thrust value for propeller 1. Following the thrust control, the balance on both sides of the quadcopter is corrected and stabilized, resulting in an approximate 6% increase in the propeller one thrust. Fig. 23(e) illustrates the effect of an obstacle moving at a velocity of 20 m/s in the x-direction on the flow of propellers rotating at 5000 rpm. The downwash generated by the propeller creates a zone of interference on the left side (propeller 2), leading to a severe separation zone that causes a decrease of 0.8% in the thrust of propeller 2. However, the thrust on propeller 1 increases by approximately 1% compared to the previous case (decrease by 5% over 15 m/s moving wall). This increase in the thrust is explained using the pressure contours illustrated in Fig. 24.

The pressure contours in Fig. 24 reveal that the pressure beneath propeller 1 is slightly lower when a moving obstacle travels at 15 m/s compared to when it moves at 20 m/s. Specifically, several pressure zones beneath propeller 1 indicate a value of 27.6 Pa for the 15 m/s moving obstacle and 38.8 Pa for the 20 m/s moving obstacle. This difference in pressure beneath the propeller results in an increase in thrust, as shown in the graph presented in Fig. 22.

E. MOVING OBSTACLE EFFECT ON TWO PROPELLERS (9550 RPM)

The thrust force variation on the propellers hovering at 9550 rpm is shown in Fig. 25. The results have shown an inconsiderable decrease in the thrust for propeller 1 by 0.8% for 10 m/s, 15 m/s, and by 2.4% for 20 m/s moving obstacle, compared to fixed wall thrust. Besides, propeller 2 experiences a slight decrease in the thrust but is insignificant compared to the previous cases when the quadcopter hovers at 3000 rpm and 5000 rpm. It is noticeable that the effect of moving walls at low and high velocities on the thrust is almost negligible when the propellers are hovering at 9550 rpm.

The reason for the variation in the thrust near a moving obstacle is depicted in Fig. 26(a), (b), (c), (d), and (e) where the velocity fields of the propellers rotating at 9550 rpm are presented in detail. Fig. 26(b) depicts the flow over the wall traveling at 5 m/s in the (x) direction, as well as the downwash generated by the propeller in both directions (x) and (−x).

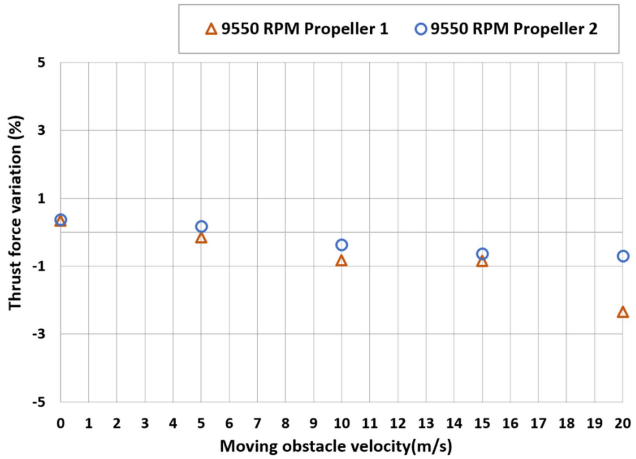

FIGURE 25. Effect of moving obstacle proximity (0.2 m) on the thrust of propeller 1 and 2 (9550 rpm).

The flows interfere on the left side of the downwash, with no obvious separating zone emerging adjacent to the propeller, causing the thrust to vary.

Fig. 26 depicts the flow over the wall moving at 10 m/s in the (x) direction, as well as the downwash generated by the propellers in both directions (x) and (−x). The flows interfere with each other somewhat between the downwash of the propellers and on the left side of propeller 1, resulting in a small fluctuation in thrust.

Fig. 26(d) depicts the flow over the obstacle moving along (x) direction at 15 m/s, and the downwash of the propellers generated in both the positive and negative (x) directions. The flows slightly interfere with each other on the left side of the downwash, resulting in a separation zone next to the propeller ($x = -1$ m), and causing a negligible decrease in the thrust.

Fig. 26(e) illustrates the effect of an obstacle moving at a velocity of 20 m/s in the x-direction on the flow of a propeller rotating at 9550 rpm. The downwash generated by the propellers creates a zone of interference on the left side, leading to a separation zone that causes a decrease of 2.4% in the thrust of propeller 1.

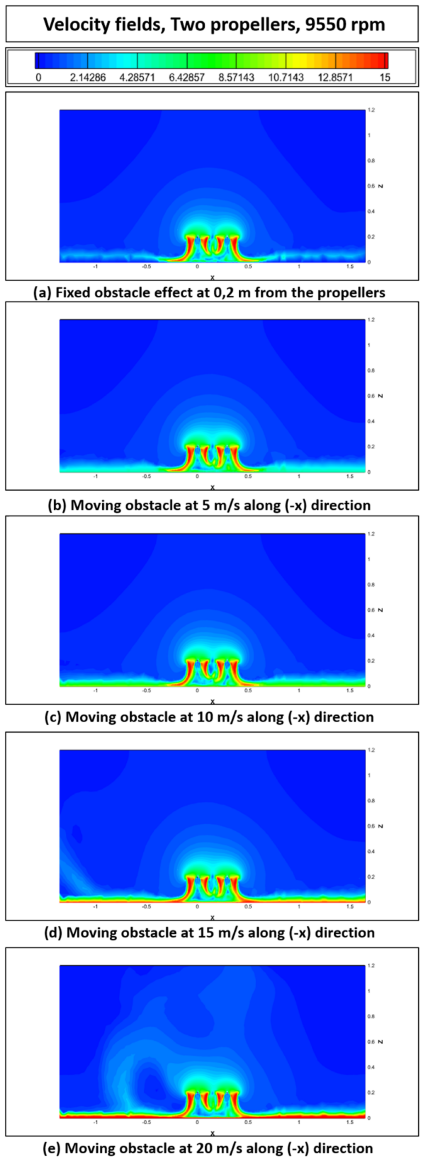

FIGURE 26. Velocity fields, 2 propellers 9550 rpm, effect of moving obstacle 5 m/s, 10 m/s, 15 m/s, and 20 m/s.

F. THRUST CONTROL AND ITS IMPACT ON POWER CONSUMPTION

In our previous discussions, we highlighted the significance of immediate thrust control for quadcopters during hovering approaches at different rpm values, specifically 3000 rpm and 5000 rpm, when in close proximity to moving vehicles moving at speeds of 15 m/s and 20 m/s. It was observed that Propeller 1, operating at 3000 rpm, encountered a significant decrease in thrust while hovering near a moving wall at 10 m/s. To ensure the stability of the UAV, the thrust control strategy was employed, leading to the appropriate increase in thrust. This section focuses on the power consumption associated with this thrust control, revealing that Propeller 1 exhibited an approximate 13% increase in power, while Propeller 2 showed a 3% slight increase.

Fig. 27 presents the power consumption of the propellers under different hovering conditions. The bars represent the power required when correcting the thrust and the moving wall is traveling at speeds of 10 m/s and 15 m/s for 3000 rpm and 5000 rpm, respectively.

As presented previously, when Propellers 1 and 2 are operating at 5000 rpm, Propeller 1 encounters a significant decrease in thrust while hovering near a moving wall at 15 m/s. To also ensure the stability of the UAV, the thrust control strategy was employed, leading to the appropriate increase in thrust. It is shown that the power consumption associated with this thrust control on propeller 1 is increased by approximately 8%.

Finally, the power consumption and thrust force data obtained from the propellers' operation will be utilized to

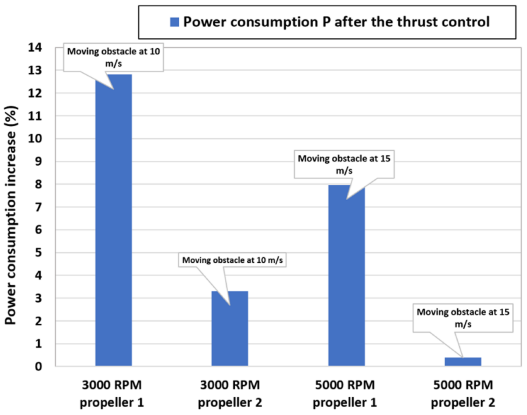

FIGURE 27. Power consumption after the thrust control of propeller 1, moving obstacle 10 m/s, 15 m/s.

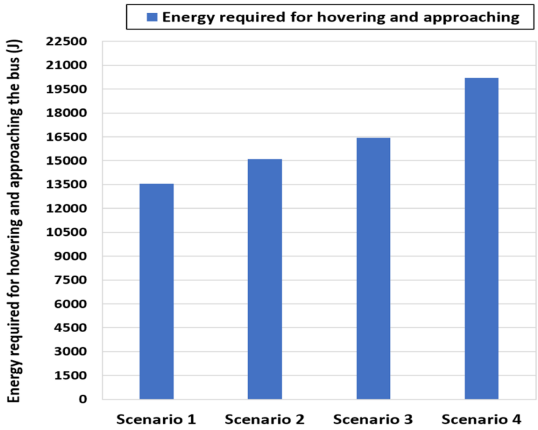

FIGURE 28. Energy required for the phantom DJI 3 for the hovering and approach phases during the flight scenarios.

improve the energy estimations required for the quadcopter hovering and approach maneuvers near moving buses or trams. Additionally, the information will enable an accurate estimation of the battery consumption levels following the UAV's flight under the varying scenarios explained previously in Section V-C. By analyzing the power consumption and the thrust force, it is possible to optimize energy usage and identify battery requirements, improving the overall operational efficiency of the quadcopter.

G. ENERGY REQUIRED AND BATTERY CONSUMPTION DURING FLIGHT SCENARIOS

Sections V-C discussed four flight scenarios for the quadcopter, including flying at cruise speed, arriving at the city center, hovering at 5000 RPM for a specific duration, and attempting to approach a moving tram by reducing propeller speed to 3000 RPM. In the first scenario, the quadcopter takes four minutes to dock onto the tram four times while in the city, with power and thrust data estimated using CFD simulations, without accounting for the increase in power required for thrust control. The last three scenarios consider this additional power required for stabilizing the quadcopter. In scenario 2, it takes five minutes to achieve docking, one minute longer than the first scenario, to ensure better correction of thrust and UAV stability.

The graph in Fig. 28 depicting the energy required for hovering and approaching the tram demonstrates that scenario two requires 10% more energy due to thrust control adjustments. Additionally, the battery consumption graph, represented in Fig. 29, shows that scenario two requires 0.63% more battery power to achieve docking compared to scenario one. These findings are significant for the overall flight delivery operation, as they highlight the importance of considering energy and battery requirements to ensure that sufficient power is available for the entire mission. It is crucial to accurately estimate energy and battery needs to avoid any operational disruptions and optimize the overall efficiency of the quadcopter.

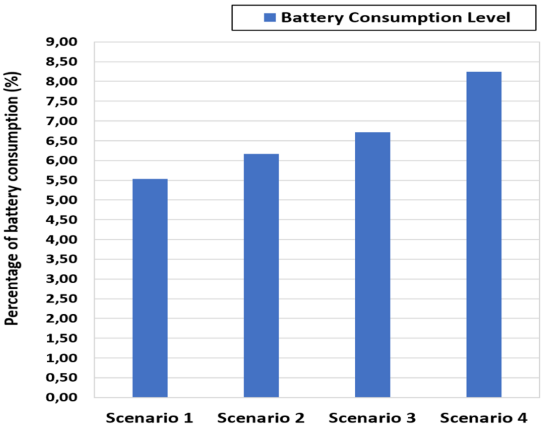

FIGURE 29. Percentage of battery consumption on the Phantom DJI 3 during the flight scenarios.

As the thrust control time increases to improve the hovering and docking stability of the quadcopter, both energy and battery consumption levels also increase. In scenario 3, which involves longer thrust control times, 9% more energy and 0.6% more battery consumption levels are required compared to scenario 2 to achieve successful flight operations.

In scenario 4, the quadcopter did not successfully approach the tram in one attempt and had to hover again for a certain period before making another attempt. This resulted in a total flight time that was 1 minute and 25 seconds longer than scenario 3. Furthermore, the energy required for scenario 4 increased by 18%, and the battery consumption level increased by 1.54% compared to scenario 3, in order to achieve a safe and successful flight scenario.

Finally, these results highlight the importance of optimizing thrust control, hovering, and approach time to minimize energy and battery consumption while ensuring the quadcopter's stability and successful mission completion. It is essential to consider such factors during flight planning to improve overall operational efficiency and avoid any potential disruptions during the UAV's operation.

VII. UAV FLIGHT REGULATIONS AND HUMAN SAFETY

Several projects, including the Deliv'Air project, are currently in preparation to utilize drones for delivering fast food and groceries. These initiatives aim to expand and develop such services for broader and more widespread use in the future. However, many social, legislative, and energy challenges are yet to be overcome before moving to any air freight transport in public areas [45]. While our article focuses on the technical aspects of propeller efficiency, we recognize the importance of safety and adherence to UAV flight regulations. Safety considerations and adherence to regulations are vital in real-world UAV operations, and it is essential to highlight and discuss these aspects to ensure the responsible use of UAV technology. Delivery drone technology does not reassure everyone, and there are several valid reasons for concern. Primarily, security issues are at the forefront of people's worries. Drones may encounter electrical or mechanical problems during flight, leading to potential accidents involving people, animals, or vehicles if they crash. Additionally, there is the risk of drone collisions with birds, buses, or cars at low altitudes, which can cause them to plummet to the ground. Furthermore, the quality of delivered packages is a significant concern. Inadequate landings or taking-off by drones on the moving buses could result in damaged packages, especially fragile items that may break upon impact. Such incidents could lead to dissatisfied customers and financial losses for businesses. Moreover, the rapid increase in delivery drone usage raises environmental and noise pollution concerns. If the skies were constantly filled with drones throughout the day, it could lead to increased noise levels and potential environmental impacts. To address these concerns and ensure wider acceptance of delivery drone technology, the Deliv'Air project will carefully consider all of these problems and takes into account the regulations implemented in France and the relevant regions to ensure safe operations. It acknowledges that more time is needed to be fully prepared for operating drones in urban areas, near buses, and trams.

VIII. CONCLUSION

This study focused on the analysis of the effect of moving vehicles on quadcopter stability during hovering and approach maneuvers, and the associated power consumption and battery requirements. The study used CFD simulations to investigate the impact of a moving wall on the thrust force generated by Phantom DJI 3 propellers. The results revealed that hovering near moving vehicles can cause significant decreases in thrust force, leading to instability in the quadcopter's flight.

To address this issue, the study also proposed a thrust force control strategy to improve the stability of the quadcopter during hovering and approach maneuvers. The strategy involved adjusting the propeller's speed to correct the thrust force and ensure the stability of the UAV. The results of the study showed that this thrust control strategy was effective in stabilizing the quadcopter during hovering and approaching maneuvers near moving vehicles. However, it also led to increased power consumption, which should be considered when estimating battery requirements for the quadcopter's operation.

The study also investigated the impact of different hovering and approach scenarios on the energy and battery requirements of the quadcopter. The results revealed that longer thrust control times led to increased energy and battery consumption levels. The study highlighted the importance of accurately estimating energy and battery needs to ensure sufficient power is available for the entire mission and to optimize the overall efficiency of the quadcopter.

Overall, this study provides valuable insights into the challenges associated with quadcopter stability during hovering and approach maneuvers near moving vehicles. The study proposes a thrust force control strategy to improve stability and highlights the importance of accurately estimating energy and battery requirements to optimize operational efficiency. These findings are significant for the development of future quadcopter systems and have the potential to improve the safety and reliability of UAV operations near moving vehicles. While our study has provided valuable insights into the landing and takeoff of quadcopters from the roofs of moving buses and trams using a planar surface wall approximation, it is crucial to acknowledge the need for further research to explore the actual flow characteristics between a complete quadcopter and an actual tram. Future studies should focus on capturing the complex flow field surrounding tramways and buses to better understand the impact on flight stability and optimize operational efficiency.

REFERENCES

[1] Y. Mai, H. Zhao, and S. Guo, "The analysis of image stabilization technology based on small-UAV airborne video," in *Proc. IEEE Int. Conf. Comput. Sci. Electron. Eng.*, 2012, pp. 586–589.

[2] G. Hoffmann, H. Huang, S. Waslander, and C. Tomlin, "Quadrotor helicopter flight dynamics and control: Theory and experiment," in *Proc. AIAA Guid., Navigation Control Conf. Exhibit*, 2007, Art. no. 6461.

[3] P. Pounds, R. Mahony, and P. Corke, "Modelling and control of a large quadrotor robot," *Control Eng. Pract.*, vol. 18, no. 7, pp. 691–699, 2010. [Online]. Available: https://www.sciencedirect.com/science/article/pii/S0967066110000456

[4] S. Dastgheibifard and M. Asnafi, "A review on potential applications of unmanned aerial vehicle for construction industry," *Sustain. Struct. Mater.*, vol. 1, no. 2, pp. 44–53, 2018.

[5] B. De Miguel Molina and M. Segarra Oña, *The Drone Sector in Europe*. Cham, Switzerland: Springer, 2018, pp. 7–33, doi: 10.1007/978-3-319-71087-7-2.

[6] H. Shakhatreh et al., "Unmanned aerial vehicles (UAVs): A survey on civil applications and key research challenges," *IEEE Access*, vol. 7, pp. 48572–48634, 2019.

[7] A. Otto, N. Agatz, J. Campbell, B. Golden, and E. Pesch, "Optimization approaches for civil applications of unmanned aerial vehicles (UAVs) or aerial drones: A survey," *Networks*, vol. 72, no. 4, pp. 411–458, 2018. [Online]. Available: https://onlinelibrary.wiley.com/doi/abs/10.1002/net.21818

[8] G. Wild, J. Murray, and G. Baxter, "Exploring civil drone accidents and incidents to help prevent potential air disasters," *Aerospace*, vol. 3, no. 3, 2016, Art. no. 22. [Online]. Available: https://www.mdpi.com/2226-4310/3/3/22

[9] F.-B. Hsiao, K.-W. Lin, M.-T. Lee, W.-Y. Chang, C.-T. Chao, and C.-F. Lin, "The design of flight stability control system and constructing simple navigation system for a long endurance autonomous UAV," in *Proc. 1st UAV Conf.*, 2002, Art. no. 3469, doi: 10.2514/6.2002-3469.

[10] P.-H. Chung, D.-M. Ma, and J.-K. Shiau, "Design, manufacturing, and flight testing of an experimental flying wing UAV," *Appl. Sci.*, vol. 9, no. 15, 2019, Art. no. 3043. [Online]. Available: https://www.mdpi.com/2076-3417/9/15/3043
[11] R. La Scalea et al., "Opportunities for autonomous UAV in harsh environments," in *Proc. IEEE 16th Int. Symp. Wireless Commun. Syst.*, 2019, pp. 227–232.
[12] R. Deters, S. Kleinke, and M. Selig, "Static testing of propulsion elements for small multirotor unmanned aerial vehicles," in *Proc. 35th AIAA Appl. Aerodynamics Conf.*, 2017, Art. no. 3743.
[13] D. Del Cont Bernard, M. Giurato, F. Riccardi, and M. Lovera, "Ground effect analysis for a quadrotor platform," in *Proc. Conf. Adv. Aerosp. Guid., Navigation, Control*, 2018, pp. 351–367.
[14] I. C. Cheeseman and W. E. Bennett, "The effect of the ground on a helicopter rotor in forward flight," 1955. [Online]. Available: https://reports.aerade.cranfield.ac.uk/handle/1826.2/3590
[15] M. Bangura et al., "Nonlinear dynamic modeling for high performance control of a quadrotor," 2012.
[16] L. Danjun, Z. Yan, S. Zongying, and L. Geng, "Autonomous landing of quadrotor based on ground effect modelling," in *Proc. IEEE 34th Chin. Control Conf.*, 2015, pp. 5647–5652.
[17] P. Sanchez-Cuevas, G. Heredia, and A. Ollero, "Characterization of the aerodynamic ground effect and its influence in multirotor control," *Int. J. Aerosp. Eng.*, vol. 2017, pp. 1–17, 2017.
[18] S. Gao, C. D. Franco, D. Carter, D. Quinn, and N. Bezzo, "Exploiting ground and ceiling effects on autonomous UAV motion planning," in *Proc. IEEE Int. Conf. Unmanned Aircr. Syst.*, 2019, pp. 768–777.
[19] X. He and K. Leang, "Quasi-steady in-ground-effect model for single and multirotor aerial vehicles," *AIAA J.*, vol. 58, no. 12 pp. 5318–5331, 2020.
[20] C. D. McKinnon and A. P. Schoellig, "Estimating and reacting to forces and torques resulting from common aerodynamic disturbances acting on quadrotors," *Robot. Auton. Syst.*, vol. 123, 2020, Art. no. 103314. [Online]. Available: https://www.sciencedirect.com/science/article/pii/S0921889018307917
[21] Y. Lei and H. Wang, "Aerodynamic optimization of a micro quadrotor aircraft with different rotor spacings in hover," *Appl. Sci.*, vol. 10, no. 4, 2020, Art. no. 1272. [Online]. Available: https://www.mdpi.com/2076-3417/10/4/1272
[22] A. Fluent et al., "Ansys fluent theory guide," Ansys Inc., USA, vol. 15317, pp. 724–746, 2011.
[23] T. Zhang, Z. Wang, W. Huang, D. Ingham, L. Ma, and M. Pourkashanian, "A numerical study on choosing the best configuration of the blade for vertical axis wind turbines," *J. Wind Eng. Ind. Aerodynamics*, vol. 201, 2020, Art. no. 104162. [Online]. Available: https://www.sciencedirect.com/science/article/pii/S0167610520300726
[24] S. Joo, H. Choi, and J. Lee, "Aerodynamic characteristics of two-bladed H-darrieus at various solidities and rotating speeds," *Energy*, vol. 90, pp. 439–451, 2015. [Online]. Available: https://www.sciencedirect.com/science/article/pii/S0360544215009469
[25] C. Paz, E. Suárez, C. Gil, and J. Vence, "Assessment of the methodology for the CFD simulation of the flight of a quadcopter UAV," *J. Wind Eng. Ind. Aerodynamics*, vol. 218, 2021, Art. no. 104776. [Online]. Available: https://www.sciencedirect.com/science/article/pii/S0167610521002543
[26] H. A. Kutty and P. Rajendran, "3D CFD simulation and experimental validation of small APC slow flyer propeller blade," *Aerospace*, vol. 4, no. 1, 2017, Art. no. 10. [Online]. Available: https://www.mdpi.com/2226-4310/4/1/10
[27] M. Stajuda, M. Karczewski, D. Obidowski, and K. Jóźwik, "Development of a CFD model for propeller simulation," *Mechanics Mech. Eng.*, vol. 20, no. 4, pp. 579–593, 2016.
[28] C. Paz, E. Suárez, C. Gil, and C. Baker, "CFD analysis of the aerodynamic effects on the stability of the flight of a quadcopter UAV in the proximity of walls and ground," *J. Wind Eng. Ind. Aerodynamics*, vol. 206, 2020, Art. no. 104378. [Online]. Available: https://www.sciencedirect.com/science/article/pii/S0167610520302889
[29] F. Schiano, J. Alonso-Mora, K. Rudin, P. Beardsley, R. Siegwart, and B. Siciliano, "Towards estimation and correction of wind effects on a quadrotor UAV," in *Proc. Int. Micro Air Veh. Conf. Competition*, 2014, pp. 134–141.
[30] T. Tomić, K. Schmid, P. Lutz, A. Mathers, and S. Haddadin, "The flying anemometer: Unified estimation of wind velocity from aerodynamic power and wrenches," in *Proc. IEEE/RSJ Int. Conf. Intell. Robots Syst.*, 2016, pp. 1637–1644.
[31] E. Smeur, G. de Croon, and Q. Chu, "Cascaded incremental nonlinear dynamic inversion for MAV disturbance rejection," *Control Eng. Pract.*, vol. 73, pp. 79–90, 2018. [Online]. Available: https://www.sciencedirect.com/science/article/pii/S0967066118300030
[32] N. Kang and M. Sun, "Simulated flowfields in near-ground operation of single and twin-rotor configurations," *J. Aircr.*, vol. 37, pp. 214–220, 2000.
[33] S. A. Raza, M. Sutherland, J. Etele, and G. Fusina, "Experimental validation of quadrotor simulation tool for flight within building wakes," *Aerosp. Sci. Technol.*, vol. 67, pp. 169–180, 2017. [Online]. Available: https://www.sciencedirect.com/science/article/pii/S1270963816311506
[34] K. Kaya and O. Özcan, "A numerical investigation on aerodynamic characteristics of an air-cushion vehicle," *J. Wind Eng. Ind. Aerodyn.*, vol. 120, pp. 70–80, 2013. [Online]. Available: https://www.sciencedirect.com/science/article/pii/S016761051300127X
[35] A. Rezaeiha, H. Montazeri, and B. Blocken, "On the accuracy of turbulence models for CFD simulations of vertical axis wind turbines," *Energy*, vol. 180, pp. 838–857, 2019. [Online]. Available: https://www.sciencedirect.com/science/article/pii/S0360544219309168
[36] B. Kakimpa et al., "CFD modelling of free-flight and auto-rotation of plate type debris," *Wind Struct.*, vol. 13, no. 2, 2010, Art. no. 169.
[37] DJI, "DJI phantom 3 standard," 2023. Accessed: Apr. 18, 2023. [Online]. Available: https://www.dji.com/fr/phantom-3-standard
[38] R. W. Deters, S. Kleinke, and M. S. Selig, "Static testing of propulsion elements for small multirotor unmanned aerial vehicles," in *Proc. 35th AIAA Appl. Aerodynamics Conf.*, 2017, Art. no. 3743, doi: 10.2514/6.2017-3743.
[39] P. Schlatter et al., "Turbulent boundary layers up to $Re_\theta = 2500$ studied through simulation and experiment," *Phys. Fluids*, vol. 21, 2009, Art. no. 051702.
[40] F. Menter, "Zonal two equation k-W turbulence models for aerodynamic flows," in *Proc. 23rd Fluid Dyn., Plasmadynamics, Lasers Conf.*, 1993, Art. no. 2906, doi: 10.2514/6.1993-2906.
[41] B. Launder and B. Sharma, "Application of energy dissipation model of turbulence to the calculation of flow near spinning disc," *Lett. Heat Mass Transfer*, vol. 1, pp. 131–137, 1974.
[42] G. Comini and S. D. Giudice, "Finite-element solution of the incompressible Navier-Stokes equations," *Numer. Heat Transfer*, vol. 5, no. 4, pp. 463–478, 1982, doi: 10.1080/10407788208913459.
[43] S. Patankar, *Numerical Heat Transfer and Fluid Flow*. New York, NY, USA: Taylor Francis, 1980, doi: 10.1201/9781482234213.
[44] DJI, "DJI phantom 3 SE unboxing: Featuring a 4K camera," DJI Official Online Store, Apr. 2023. Accessed: Apr. 18, 2023. [Online]. Available: https://store.dji.com/guides/dji-phantom-3-se-unboxing-featuring-a-4k-camera/
[45] C. Stöcker, R. Bennett, F. Nex, M. Gerke, and J. Zevenbergen, "Review of the current state of UAV regulations," *Remote Sens.*, vol. 9, no. 5, 2017, Art. no. 459. [Online]. Available: https://www.mdpi.com/2072-4292/9/5/459

CHARBEL HAGE received the graduation degree from Polytech Orléans, Orléans, France, in 2021. He is currently working toward the Ph.D. degree with the University of Burgundy's DRIVE Lab, Nevers, France. He is also a CFD Engineer with a focus on energy management and optimization. His research focuses on utilizing CFD simulations to optimize energy management systems for sustainable transportation solutions. He is developing a multimodal delivery system that utilizes drones and existing public transport infrastructure to reduce the carbon footprint of transportation systems. He is committed to environmental sustainability and is passionate about utilizing engineering concepts to tackle real-world challenges. With his expertise in CFD simulations, he strives to develop practical and sustainable solutions that can help reduce the impact of transportation on the environment.

TONINO SOPHY has been an Assistant Professor with the Automotive and Transportation Superior Institute of Nevers (ISAT), University of Burgundy, Nevers, France, since September 2004, where he actually heads the training department. After an experimental work on the performance of heat pipes with the Laboratoire d'etudes Thermiques in Poitiers in 1998, he defended his Ph.D. thesis on MHD/CFD coupling using a meshless method in the same laboratory in 2002. He now contributes to numerical energetic studies (mainly for transportation issues) with the DRIVE laboratory.

EL-HASSANE AGLZIM has been currently a Full Professor with theDRIVE Laboratory Département de Recherche en Ingénierie des Véhicules pour l'Environnement, University of Burgundy, Nevers, France, since 2020. His research interests include battery and energy optimization/management in electric and hybrid vehicles, fuel cells, and autonomous vehicle. In parallel to his research works, he teaches electrical engineering, signal acquisition, electrical motors, and hybrid/electric vehicles. He heads the Energetic and Autonomous Vehicles Department, ISAT Engineering School, Institut Supérieur de l'Automobile et des Transports, and also the Smart and Connected Systems Research Team of the DRIVE Laboratory.